J. Fluid Mech. (2014), *vol.* 756, *pp.* 488–509. © Cambridge University Press 2014
doi:10.1017/jfm.2014.457

Evolution of a turbulent cloud under rotation

A. Ranjan[1,†] **and P. A. Davidson**[1]

[1]Department of Engineering, University of Cambridge, Cambridge CB2 1PZ, UK

(Received 22 November 2013; revised 25 July 2014; accepted 4 August 2014;
first published online 2 September 2014)

Localized patches of turbulence frequently occur in geophysics, such as in the atmosphere and oceans. The effect of rotation, $\boldsymbol{\Omega}$, on such a region (a 'turbulent cloud') is governed by inhomogeneous dynamics. In contrast, most investigations of rotating turbulence deal with the homogeneous case, although inhomogeneous turbulence is more common in practice. In this paper, we describe the results of 512^3 direct numerical simulations (DNS) of a turbulent cloud under rotation at three Rossby numbers (Ro), namely 0.1, 0.3 and 0.5. Using a spatial filter, fully developed homogeneous turbulence is vertically confined to the centre of a periodic box before the rotation is turned on. Energy isosurfaces show that columnar structures emerge from the cloud and grow into the adjacent quiescent fluid. Helicity is used as a diagnostic and confirms that these structures are formed by inertial waves. In particular, it is observed that structures growing parallel to the rotation axis (upwards) have negative helicity and those moving antiparallel (downwards) to the axis have positive helicity, a characteristic typical of inertial waves. Two-dimensional energy spectra of horizontal wavenumbers, $k_\perp$, versus dimensionless time, $2\Omega t$, confirm that these columnar structures are wavepackets which travel at the group velocities of inertial waves. The kinetic energy transferred from the turbulent cloud to the waves is estimated using Lagrangian particle tracking to distinguish between turbulent and 'wave-only' regions of space. The amount of energy transferred to waves is 40 % of the initial at $Ro = 0.1$, while it is 16 % at $Ro = 0.5$. In both cases the bulk of the energy eventually resides in the waves. It is evident from this observation that inertial waves can carry a significant portion of the energy away from a localized turbulent source and are therefore an efficient mechanism of energy dispersion.

Key words: rotating flows, rotating turbulence, waves in rotating fluids

1. Introduction

Rotating turbulent flows are routinely encountered not only in geophysics but also in turbomachinery, and therefore interest meteorologists and engineers alike. Turbulence in the atmosphere is primarily inhomogeneous in at least one direction (Wilson, Thurtell & Kidd 1981). Moreover, localized patches of turbulence subjected to rotation frequently occur in the atmosphere and oceans (Haine & Cherian 2013). Understanding such flows is important for many meteorological, geological and engineering applications. There have been numerous theoretical and numerical investigations of rotating turbulent flows, most of which pertain to the homogeneous

† Email address for correspondence: ar606@cam.ac.uk

https://doi.org/10.1017/jfm.2014.457 Published online by Cambridge University Press

case. For our study, we consider a freely decaying localized region of turbulence with quiescent fluid above and below, hereafter referred to as a 'turbulent cloud'. This is an example of unbounded turbulence governed by inhomogeneous dynamics. Rotation and stratification co-exist in many geophysical phenomena, and have close analogies (Veronis 1970). A turbulent cloud under the effect of stratification has recently been investigated by Maffioli *et al.* (2014). In this study, we consider rotation alone which is particularly relevant to the equatorial plane in the core of the Earth, where a pronounced radial heat flux is thought to be a localized source of turbulence and hence inertial waves (Olson 2013; Davidson 2014).

Momentum conservation for an incompressible fluid in the non-inertial rotating frame of reference includes the Coriolis force $2\boldsymbol{u}\times\boldsymbol{\Omega}$:

$$\frac{\partial \boldsymbol{u}}{\partial t}+(\boldsymbol{u}\cdot\boldsymbol{\nabla})\boldsymbol{u}=-\boldsymbol{\nabla}\left(\frac{\tilde{p}}{\rho}\right)+2\boldsymbol{u}\times\boldsymbol{\Omega}+\nu\nabla^2\boldsymbol{u}, \tag{1.1}$$

where $\tilde{p}$ is the modified pressure which incorporates the centrifugal force and $\boldsymbol{\Omega}=\Omega\hat{\boldsymbol{e}}_z$. The relative importance of inertial and Coriolis forces is characterized by the Rossby number, $Ro=u/2\Omega l$, where u and l are characteristic velocity and length scales, respectively. For small Ro, the Coriolis force can sustain internal waves known as inertial waves. These waves produced by Earth's rotation have been detected in the stratosphere (Thompson 1978). In an inviscid fluid subjected to high rotation rates, these waves are known to create fluid columns above and below a slowly moving object which translate with the object (Lighthill 1967). These columnar structures, called Taylor columns, were predicted by Proudman (1916) and observed in the experiments of Taylor (1921). Moreover, Greenspan (1968) has shown that Taylor columns are formed by the propagation of low-frequency inertial waves along the rotation axis.

Let us briefly review some of the important properties of inertial waves. For an inviscid, incompressible fluid at low Ro, the vorticity equation is

$$\frac{\partial \boldsymbol{\omega}}{\partial t}=2(\boldsymbol{\Omega}\cdot\boldsymbol{\nabla})\boldsymbol{u}, \tag{1.2}$$

from which we obtain

$$\frac{\partial^2}{\partial t^2}(\nabla^2\boldsymbol{u})+4(\boldsymbol{\Omega}\cdot\boldsymbol{\nabla})^2\boldsymbol{u}=0. \tag{1.3}$$

This equation supports plane waves of the form $\boldsymbol{u}=\hat{\boldsymbol{u}}\exp[\mathrm{i}(\boldsymbol{k}\cdot\boldsymbol{x}-\varpi t)]$ when $\varpi^2<4\Omega^2$. These are inertial waves for which the dispersion relation and group velocity are

$$\varpi=\pm 2(\boldsymbol{k}\cdot\boldsymbol{\Omega})/k, \tag{1.4}$$

$$\boldsymbol{C}_g=\pm\left[\frac{2\boldsymbol{\Omega}}{k}-\frac{2(\boldsymbol{k}\cdot\boldsymbol{\Omega})k}{k^3}\right]. \tag{1.5}$$

The waves of low frequency, for which $(\boldsymbol{k}\cdot\boldsymbol{\Omega})\approx 0$, propagate with the highest group velocity and in a direction parallel to $\boldsymbol{\Omega}$, $\boldsymbol{C}_g=\pm 2\boldsymbol{\Omega}/k$. On the other hand, the highest-frequency waves, $\varpi=\pm 2\Omega$, do not disperse energy. Using (1.2) and (1.4), vorticity in a plane inertial wave can be expressed as

$$\hat{\boldsymbol{\omega}}=\mathrm{i}\boldsymbol{k}\times\hat{\boldsymbol{u}}=\mp k\hat{\boldsymbol{u}}. \tag{1.6}$$

https://doi.org/10.1017/jfm.2014.457 Published online by Cambridge University Press

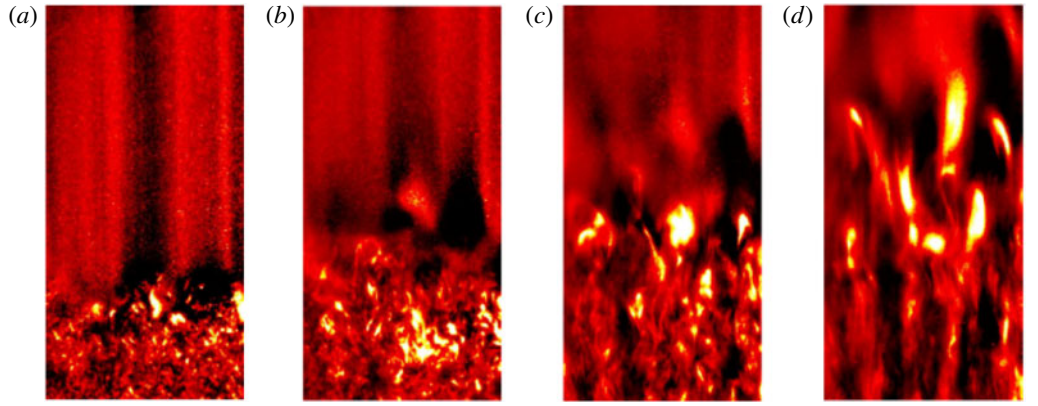


FIGURE 1. (Colour online) Turbulent cloud under rotation: reflected light intensity at (*a*) $\Omega t = 1.1$, (*b*) $\Omega t = 6.0$, (*c*) $\Omega t = 11.0$ and (*d*) $\Omega t = 15.9$ (Davidson, Staplehurst & Dalziel 2006; Staplehurst 2007).

Since, $\boldsymbol{u}$ and $\boldsymbol{\omega}$ are parallel, inertial waves are circularly polarized helical waves. They posses helicity (strictly speaking helicity density) given by

$$h = \hat{\boldsymbol{u}} \cdot \hat{\boldsymbol{\omega}} = \mp k u^2. \tag{1.7}$$

Evidently, inertial waves that propagate upwards ($+z$) have negative helicity where as those that propagate downwards ($-z$) have positive helicity (Moffatt 1970). Helicity has been used as a dynamic parameter in the context of atmospheric fluid flow (Zhemin & Rongsheng 1994), rotating thunderstorms (Lilly 1986), in the study of homogeneous turbulence (Mininni & Pouquet 2010) and as a diagnostic to detect inertial waves (Davidson 2013).

Large-scale columnar vortices parallel to the rotation axis have been observed in many experimental investigations of rotating turbulence, with the columnar vortices emerging spontaneously from the turbulence. Typical of these are rotating tank experiments of Hopfinger, Browand & Gagne (1982), Dickinson & Long (1983) and, more recently, Davidson *et al.* (2006) and Kolvin *et al.* (2009). One of the earliest visualizations of inhomogeneous rotating turbulence was by Hopfinger *et al.* (1982) who used an oscillating grid in a rotating tank. They observed a quasi-two-dimensional field of concentrated columnar vortices some distance away from the grid where the local Ro was 0.2. In a similar flow visualization experiment using an oscillating grid, Dickinson & Long (1983) characterized the rate of spread of the turbulent fluctuations. For $Ro < 1$, the speed of the turbulent wavefront is found to be proportional to the group velocity of zero-frequency inertial waves. This was one of the first observations consistent with the idea that turbulent kinetic energy can spread by wave propagation. However, due to the continuous forcing, the grid itself could be a source of waves in this experiment, over and above those waves created by the turbulence.

To overcome this, Davidson *et al.* (2006) conducted experiments in which turbulence was produced by a single grid oscillation at large Ro and then left to decay. Figure 1 shows the reflected light intensity at different times after the start of rotation in which the emergence of columnar structures is seen for $\Omega t > 11$. It was found that these columnar vortices grew at a rate consistent with the group velocity of low-frequency waves, $\boldsymbol{C}_g = 2\boldsymbol{\Omega}/k$, despite the fact that these columns

https://doi.org/10.1017/jfm.2014.457 Published online by Cambridge University Press

were observed at $Ro \sim 1$, where both inertial and Coriolis forces are relevant. In a similar experiment, Kolvin *et al.* (2009) conducted planar particle image velocimetry (PIV) in a rotating tank, in which turbulence was created using water injection through a grid. They defined two time scales, namely the linear time scale given by $\tau_L = hk/2\Omega$, and the nonlinear time scale given by $\tau_{NL} = (uk)^{-1}$, where k, h, u are the wavenumber, the characteristic height of experiment and the root-mean-square (r.m.s.) velocity, respectively. Like Davidson *et al.* (2006), they observed energy propagating away from the disturbance at a speed consistent with linear inertial waves, despite the fact that $Ro \sim 1$. However, vertical confinement is important in their experiment and in fact τ_L is a measure of the time taken by inertial waves to traverse the tank. Indeed, Kolvin *et al.* (2009) suggested that spectral energy evolves beyond $t > \tau_L$ by nonlinear dynamics.

There are several nonlinear theories of rotating turbulence including the resonant-triad interactions theory of Waleffe (1993) which applies for $Ro \ll 1$, and the strong turbulence theory of Nazarenko & Schekochihin (2011) which applies for $Ro \sim 1$. A nonlinear transfer of energy to horizontal wavenumbers over large time ($t \geqslant \tau_{NL}$) has been observed in both freely decaying (Cambon & Jacquin 1989; Jacquin *et al.* 1990; Bartello, Métais & Lesieur 1994; Cambon, Mansour & Godeferd 1997) and forced (Yeung & Zhou 1998; Smith & Waleffe 1999; Smith & Lee 2005) homogeneous rotating turbulence at $Ro < 1$. Based on the weak turbulence theory, Bellet *et al.* (2006) developed a wave-turbulence model for rapidly rotating flows which has now been applied to channel flows by Scott (2014). In an experiment using PIV (Bordes *et al.* 2012), inertial waves of a fixed frequency were generated by an oscillating wave-maker in a rotating fluid. By measuring the frequencies and wavevectors of the secondary waves, excited by subharmonic instability, they provide evidence of the triadic resonance of inertial waves. In a similar study by Duran-Matute *et al.* (2013) using PIV and direct numerical simulations (DNS), inertial wave cones were generated using an oscillating torus. They observed that inertial wave focusing leads to angular momentum mixing which in turn leads to a nonlinear transfer of energy to form a columnar vortex. However, the freely decaying homogeneous experiments of Staplehurst, Davidson & Dalziel (2008) showed that two-point correlations based on vorticity collapse to a single curve on being normalized by Ω and a characteristic horizontal length scale, suggesting that the large scales continue to elongate by linear wave propagation for $t > \tau_L$.

In a recent study, Yoshimatsu, Midorikawa & Kaneda (2011) attempted to quantify the roles of the linear and nonlinear dynamics in the formation of columnar structures in freely decaying homogeneous rotating turbulence at $Ro \sim 1$. They obtained DNS of the Navier–Stokes equations with rotation, and also for a series of artificial fields obtained by ignoring the advection and viscous dissipation terms. They concluded that the nonlinear energy transfer is essential in order to sustain the increase in integral length scale parallel to the rotation axis observed in homogeneous rotating turbulence. In addition, Yoshimatsu *et al.* (2011) simulated localized eddies under rotation and concluded that arriving at a proper definition of the length scale to characterize the elongating eddies is rather difficult. Furthermore, they emphasized on the need to characterize the role of linear inertial waves in the formation of columnar structures.

There is a notable contrast between the Taylor columns created by slowly moving a solid object through a quiescent, rotating fluid and the columnar structures observed in the experiments on rotating turbulence, although inertial waves play a role in both cases. On the one hand, the classical explanation for Taylor column formation relies on a slowly moving object generating low-frequency waves (Greenspan 1968),

https://doi.org/10.1017/jfm.2014.457 Published online by Cambridge University Press

since it is only the low-frequency waves which travel along the rotation axis. On the other hand, the spontaneous growth of columnar structures from a cloud of turbulence has no imposed time scale. Davidson *et al.* (2006) have shown that despite these differences, the two phenomena are closely related, at least at low *Ro*. They considered the case of a localized disturbance at low *Ro*. They showed that the confinement of the axial component of angular momentum of the disturbance results in a focusing of the dispersed wave energy, preferentially channelling the kinetic energy along the rotation axis. This is a general result which can explain the formation of elongated columnar structures at low *Ro* in the absence of any imposed time scale.

As discussed above, many researchers argue that nonlinear dynamics is important for the growth of long-lived columnar structures in the case of homogeneous rotating turbulence. However, this does not necessarily apply to inhomogeneous turbulence. For example, in a DNS study of rotation with confinement, Godeferd & Lollini (1999) observed that the columnar structuring of the flow occurs 'abruptly', predominantly due to Ekman pumping and linear wave propagation, as opposed to a 'slow' nonlinear transfer of energy observed in homogeneous turbulence. In the case of unbounded inhomogeneous turbulence, we suspect that inertial waves have a role to play in the spontaneous generation of columnar structures, particularly in the short linear time scale Ω^{-1}. In the present study we conduct a DNS of a freely decaying turbulent cloud under rotation to investigate the following questions. (*a*) What exactly is the role of inertial waves and how do they create columnar structures? (*b*) How much kinetic energy do the waves carry? (*c*) What is the effect of a change in *Ro*? The methodology adopted in the present study is described in detail in § 2. The results obtained from the DNS are discussed in § 3 in subsections on energy isosurfaces, elongation and size of columnar structures, particle tracking and wave energetics. We conclude in § 4.

2. Methodology

The DNS code used in the present work employs the pseudo-spectral method based on the discrete Fourier transform (DFT) defined as

$$\hat{\boldsymbol{u}}(\boldsymbol{k}) = \frac{1}{N^3}\sum_{N_x=1}^{N-1} \boldsymbol{u}(\boldsymbol{N}_x)\exp(-\mathrm{i}\boldsymbol{k}\cdot\boldsymbol{x}), \tag{2.1}$$

where, $\boldsymbol{N}_x = (N/2\pi)\boldsymbol{x}$, $N = 512$. The numerical domain of interest is a N^3 periodic box of size $l_{box} = 2\pi$. The code solves the momentum (1.1) in rotating frame written in Fourier space (Yeung & Zhou 1998) as

$$\frac{\partial \hat{u}_i}{\partial t} + \nu k^2 \hat{u}_i = -P_{ij}\hat{G}_j - 2P_{ij}\epsilon_{j3m}\Omega\hat{u}_m, \tag{2.2}$$

where $P_{ij} = (\delta_{ij} - k_i k_j/k^2)$ is the projection tensor, $\hat{G}_j$ is the DFT of the advection term $u_j\partial u_i/\partial x_j$, $\boldsymbol{\Omega} = \Omega\hat{\boldsymbol{e}}_z$ and ϵ_{ijk} is the Levi-Civita tensor. The DNS code is based on Rogallo's pseudo-spectral algorithm (Rogallo 1981) with time advancement using second-order Runge–Kutta predictor–corrector scheme. Moreover, an integrating factor which includes rotation in addition to the viscous terms (Yeung & Zhou 1998) is incorporated in the code. The de-aliasing of nonlinear terms is carried out using phase-shifting and truncation (i.e. all modes with $k > 2^{1/2}N/3$ are truncated).

https://doi.org/10.1017/jfm.2014.457 Published online by Cambridge University Press

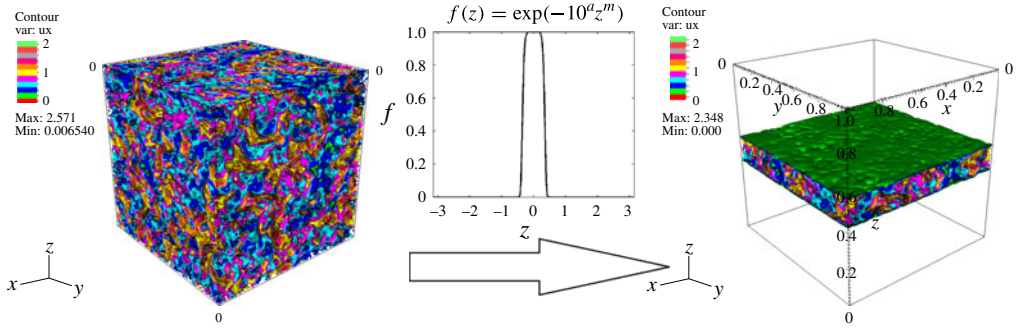


FIGURE 2. (Colour online) Creating a turbulent cloud using a spatial filter $f(z) = \exp(-10^a z^m)$ where $a = 4$ and $m = 9$.

Resolution	k_p	k_{max}/k_p	l_{box}/l_0	Re_0	ν
512^3	15	16	35	140	0.001

TABLE 1. Simulation parameters for the homogeneous precomputation, where l_0 is the integral length scale at the end of the precomputation and Re_0 is the corresponding Reynolds number.

2.1. *Initial conditions*

The initial turbulent cloud is created by a two-step procedure: (*a*) first, a precomputation of homogeneous turbulence in a periodic box is performed until the turbulence is fully developed; (*b*) subsequently, turbulence is confined vertically to the centre of the box using a spatial filter. The homogeneous precomputation is initialized with random modes satisfying the Batchelor spectrum for low wavenumbers, $E(k) \sim k^4 \exp(-2k^2/k_p^2)$ where k_p is the location of the peak. The simulation parameters are given in table 1. The turbulence is deemed to be fully developed when the skewness of the one-dimensional velocity gradient reaches a constant value of -0.5 ± 0.05. The value of $k_{max}\eta = 1.01$, where η is the Kolmogorov scale and k_{max} is the maximum wavenumber after truncation, indicates that all scales are adequately resolved. An exponential spatial filter $f(z) = \exp(-10^a z^m)$ is used to confine the turbulence to the centre of the box as indicated in a schematic (figure 2). The thickness of the cloud, $l_c = 0.11 l_{box}$, is approximately four times the integral length scale at the end of the precomputation, l_0. The filter used is smooth at the edges in order to avoid the oscillations caused by Gibbs' phenomenon (Pan 2001). Using a smooth filter seems reasonable because in the inhomogeneous rotating tank experiments (Davidson *et al.* 2006), where turbulence is created by a single grid oscillation, the transition between the turbulent and quiescent regimes is gradual and not abrupt. The DNS of the rotating turbulent cloud is then carried out, with the filtered velocity field as input, at three Rossby numbers, namely 0.1, 0.3 and 0.5. The simulation parameters for these DNS cases are provided in table 2.

2.2. *A validation of the code using a deterministic example*

To test the accuracy of the DNS code used in the present study, we consider the case of a Gaussian eddy with its axis parallel to $\boldsymbol{\Omega}$, for which Davidson *et al.* (2006) have

https://doi.org/10.1017/jfm.2014.457 Published online by Cambridge University Press

Case	Resolution	Ro	2Ω	l_c/l_{box}	l_{box}/l_0	l_c/l_0
R0.1	512^3	0.1	37.0	0.11	35.9	4
R0.3	512^3	0.3	12.3	0.11	35.9	4
R0.5	512^3	0.5	7.40	0.11	35.9	4

TABLE 2. Simulation parameters for the DNS of turbulent cloud, where $Ro = u/2\Omega l_0$.

obtained an analytical solution. In polar coordinates (r, θ, z), the initial velocity field is given by

$$\boldsymbol{u} = \Lambda r \exp\left(-\frac{r^2+z^2}{\delta^2}\right)\hat{\boldsymbol{e}}_\theta, \tag{2.3}$$

where δ is the characteristic size and Λ is the characteristic angular rotation rate. The solution of the wave equation, i.e.

$$\frac{\partial^2}{\partial t^2}\left[r\frac{\partial}{\partial r}\frac{1}{r}\frac{\partial(ru_\theta)}{\partial r} + \frac{\partial^2(ru_\theta)}{\partial z^2}\right] + 4\Omega^2\frac{\partial^2(ru_\theta)}{\partial z^2} = 0, \tag{2.4}$$

which supports inertial waves, with (2.3) as the initial condition, is given as

$$u_\theta = \frac{\Lambda\delta^5}{8\pi^{1/2}}\int_0^\infty k_r^2 \exp\left[\frac{-k_r^2\delta^2}{4}\right] \mathrm{J}_1(k_r r) I(k_r)\,\mathrm{d}k_r, \tag{2.5}$$

where J_1 is a Bessel function of the first kind, and

$$I(k_r) = \int_0^\infty \exp\left[\frac{-k_z^2\delta^2}{4}\right]\left[\cos\left(k_z\left(z-\frac{2\Omega t}{k}\right)\right) + \cos\left(k_z\left(z+\frac{2\Omega t}{k}\right)\right)\right]\mathrm{d}k_z. \tag{2.6}$$

From the solution (2.5), it was shown by Davidson *et al.* (2006) that the wave kinetic energy preferentially disperses along z-axis forming columnar structures with centres at $z \sim \pm\delta\Omega t$ and the length scale grows as $l_z \sim \delta\Omega t$. We obtain a solution of (2.5) for an eddy ($\delta = 0.125$, $\Lambda = 2.5$) using Gauss–Konrod quadrature. With the same initial conditions, a DNS of the evolution of a Gaussian eddy under rotation is conducted at $Ro \sim 0.1$. At $2\Omega t = 24$, the contours of ${u_\theta}^2$ obtained from the analytical solution are shown in figure 3(*a*). This can be compared with the corresponding ${u_\theta}^2$ contours in the x–z plane passing through axis of the eddy, obtained from the DNS, as shown in figure 3(*b*). In both plots, ${u_\theta}^2$ is normalized by its corresponding maximum value. There is a good agreement between the two, even though there is viscous dissipation present in the DNS unlike the analytical solution.

3. Results and discussion

3.1. *Energy isosurfaces*

3.1.1. *Case R0.1*

The results obtained from the DNS of the turbulent cloud are visualized in terms of velocity and energy isosurfaces. Figure 4(*a–e*) shows the isosurfaces of the velocity component along the z-axis, u_z, for $2\Omega t = 0$–16 for R0.1. Columnar flow structures are seen to emerge from the cloud, and grow vertically into the quiescent fluid. These are qualitatively similar to the flow structures observed in the experiments of

https://doi.org/10.1017/jfm.2014.457 Published online by Cambridge University Press

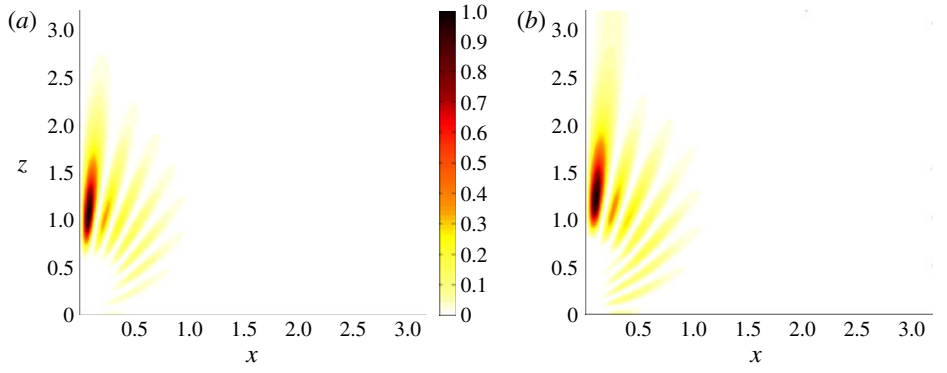


FIGURE 3. Contours of $u_\theta{}^2/(u_\theta{}^2)_{max}$: (*a*) analytical solution of (2.5) and (*b*) in the x–z plane passing through the axis of the Gaussian eddy obtained from the DNS, at $2\Omega t = 24$.

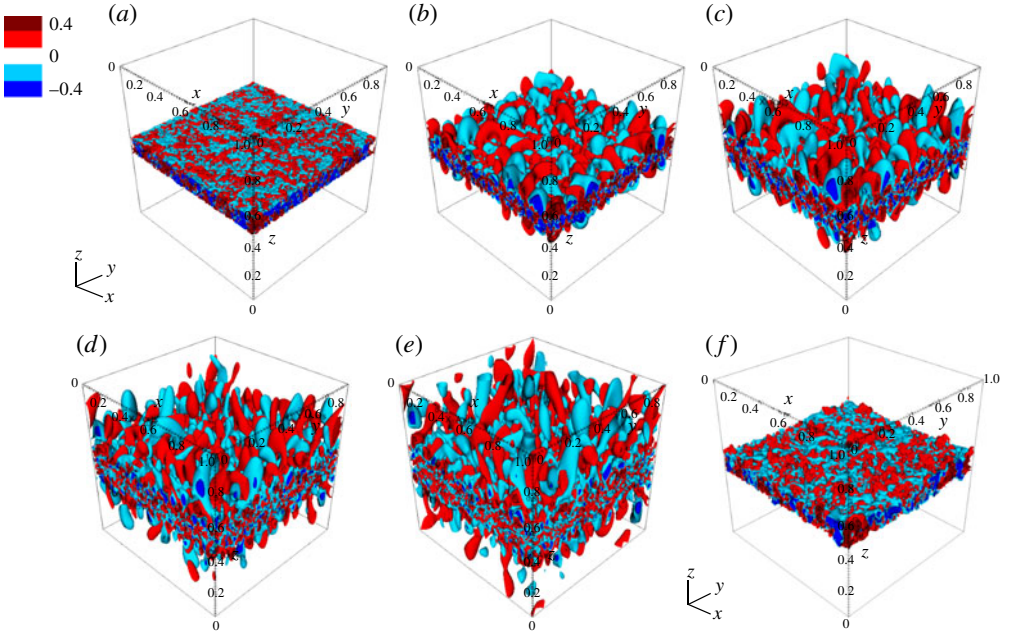


FIGURE 4. Isosurfaces of u_z at $2\Omega t =$ (*a*) 0 (*b*) 4 (*c*) 8 (*d*) 12 (*e*) 16 for the case R0.1 (red and blue colours respectively denote the positive and negative values of u_z). (*f*) With rotation absent, isosurfaces of u_z at time $t = 0.45$ (corresponds to $2\Omega t = 16.6$ for the case R0.1, see table 2).

Davidson *et al.* (2006) shown earlier in figure 1. Moreover, these structures are not observed if rotation is absent. This is evident by comparing figure 4(*e*,*f*), which show the isosurfaces of u_z with and without rotation, respectively at the same absolute time. At this point we might ask: is the formation of these columnar structures due to linear inertial wave propagation?

As discussed earlier (§ 1, (1.7)), an important characteristic of the inertial waves is that the waves propagating parallel to the rotation axis have positive helicity and those anti-parallel have negative helicity. To see if this applies to our problem, we compute

https://doi.org/10.1017/jfm.2014.457 Published online by Cambridge University Press

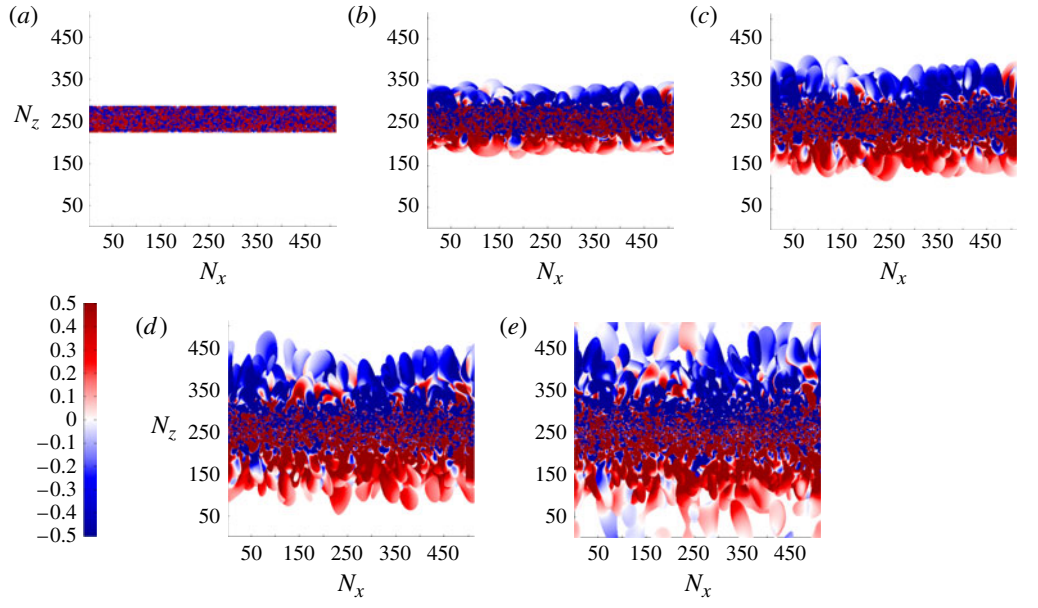


FIGURE 5. The isosurfaces of $u_z^2 = 0.05$ (front view) coloured with helicity (red denotes positive helicity and blue denotes negative) at (*a*) $2\Omega t = 0$, (*b*) $2\Omega t = 4$, (*c*) $2\Omega t = 8$, (*d*) $2\Omega t = 12$ and (*e*) $2\Omega t = 16$ for the case R0.1.

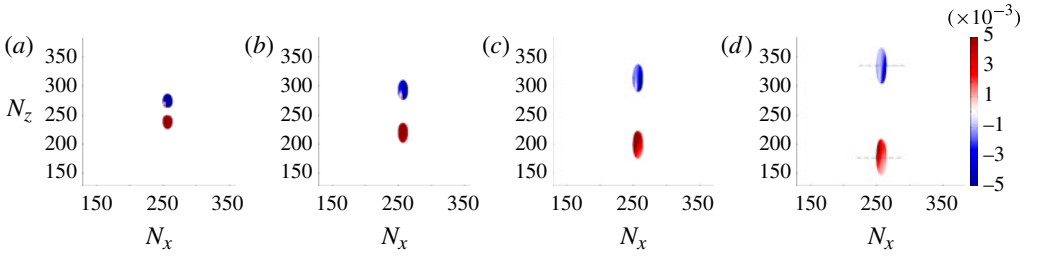


FIGURE 6. Evolution of a Gaussian eddy: isosurfaces of $u_z^2/(u_z^2)_{max} = 0.2$ coloured with helicity (red denotes positive helicity and blue denotes negative) at (*a*) $2\Omega t = 4$, (*b*) $2\Omega t = 8$, (*c*) $2\Omega t = 12$ and (*d*) $2\Omega t = 16$. Note that – – – indicates the mid-plane of the wavepacket.

helicity from the velocity and vorticity data obtained from the DNS in the entire simulation domain. The isosurfaces of $u_z^2 = 0.05$, coloured with the corresponding helicity, are shown in figure 5(*a–e*) for $2\Omega t = 0$–16. These plots clearly show that most of the columnar structures that propagate along $+z$ have negative helicity and those that propagate along $-z$ have positive helicity. It is useful to note that this characteristic was also observed for an elongating Gaussian eddy, see figure 6 at $2\Omega t \geqslant 12$ (note the resemblance between the shape of the elongated eddy and the flow structures that arise from the turbulent cloud). At late times the energy dispersion pattern in figure 6 resembles a wavepacket whose mid-plane propagates axially at the rate $C_g = 2\Omega/k_\perp \sim 2\Omega\delta$, but whose overall length increases as $l_z \sim 2\Omega\delta t$ (Davidson *et al.* 2006). Thus, the top of the wavepacket travels faster than the mid-plane, while the bottom travels slower. We shall return to this point shortly.

https://doi.org/10.1017/jfm.2014.457 Published online by Cambridge University Press

The plot at $2\Omega t = 16$ (figure 5*e*) shows that many columnar structures have reached the periodic box boundary, and so we stop the simulation at this time. From these plots, it is evident that the columnar structures are formed by packets of low-frequency inertial waves which have a major component of their group velocity along the z-axis. A rough estimate of their group speed is given by $C_g \sim 2\Omega l_0$, l_0 being the integral length scale. This suggests that the columnar structures should reach the box boundary in a non-dimensional saturation time of

$$2\Omega t_s \sim \frac{(l_{box} - l_c)}{2l_0} \sim 15.9. \tag{3.1}$$

Indeed, in the DNS visualizations we find that most of the flow structures reach the boundary by $2\Omega t_s = 16$. It is useful to note that this time corresponds to just over one nonlinear eddy turnover time, at $Ro = 0.1$ since $Ro = \tau_{NL}/2\Omega t$. Clearly, this time is too short for the nonlinear dynamics to play any significant role in the formation of columnar structures in this study.

In figure 5(*a–e*) there are occasional regions of opposite sign helicity, i.e. regions of positive helicity (shown in red) above the cloud, and negative helicity below the cloud (in blue). This observation can be explained by the fact that we have many wavepackets propagating upward (or downward), some of which overlap, and the rule that h has the same sign as $-\boldsymbol{C_g} \cdot \boldsymbol{\Omega}$ applies strictly to single Fourier modes only. In order to get a quantitative picture of the helicity propagation, we compute the total negative and positive helicity in all of the horizontal (x–y) planes (defined by $1 < N_z < 512$, where $N_z = 512(z/2\pi)$) as shown in figure 7. Once again, it is evident that the helicity propagation is typical of inertial waves. Moreover, there is a symmetry in the positive and negative helicity curve shapes which indicates that total helicity is approximately constant with time. It is interesting to note that a clear bias for the helicity direction exists even inside the turbulent cloud. This indicates the presence of inertial waves arising from within the cloud itself.

3.1.2. *Cases R0.3 and R0.5*

Do the columnar structures emerge and grow at a higher Ro? To address this, we consider the results from the DNS of a turbulent cloud at $Ro = 0.3$, 0.5. The u_z-isosurfaces for the case R0.3 are shown in figure 8 (the numerical threshold of contour levels in this figure are half those used for the case R0.1 since the r.m.s. velocity is lower by 50 % at $2\Omega t = 16$). Even at a higher Ro, the columnar structures are seen to emerge from the turbulent cloud and grow towards the box boundary. This is observed even for the case R0.5 as discussed below. Most structures appear to reach the box boundary at $2\Omega t = 12$, i.e. earlier as compared with the time taken in the case R0.1 ($2\Omega t = 16$), although this may be just an artifact of a lower threshold. Similar to the case R0.1, the helicity colour is predominantly negative (blue) and positive (red) in the $+$ and $-z$ direction respectively, for both cases R0.3 and R0.5 (figures 9–11). Moreover, the positive/negative helicity propagation is once again symmetric (figure 11).

3.2. *Elongation, propagation and size of columnar structures*

The elongation rate of the columnar structures provides another way to test whether they form through linear wave propagation. Using two-dimensional boundary tracking applied to the front or side view of $|u_z|$ isosurfaces we can estimate the extent of the growing columnar cloud region (figure 12*a*), hereafter referred to as the wave-cloud

https://doi.org/10.1017/jfm.2014.457 Published online by Cambridge University Press

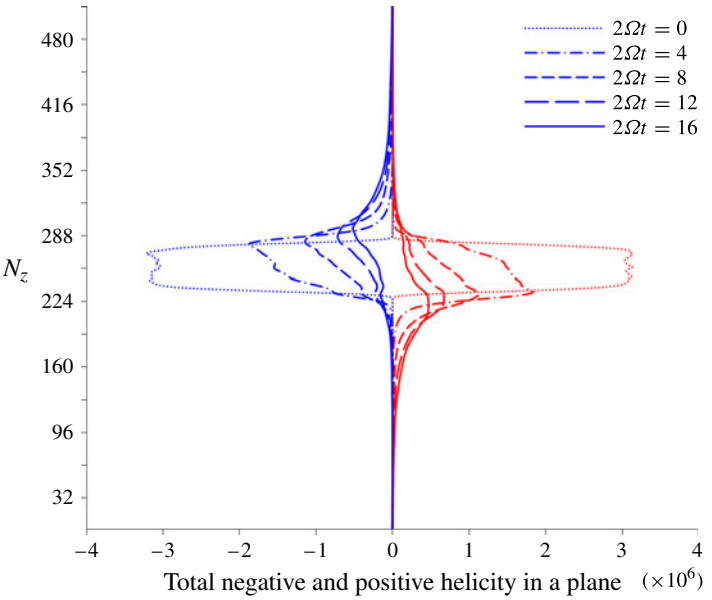


FIGURE 7. Total negative and positive helicity in horizontal planes $1 < N_z < 512$, where $N_z = N(z/2\pi)$ (red denotes positive helicity and blue denotes negative) for the case R0.1.

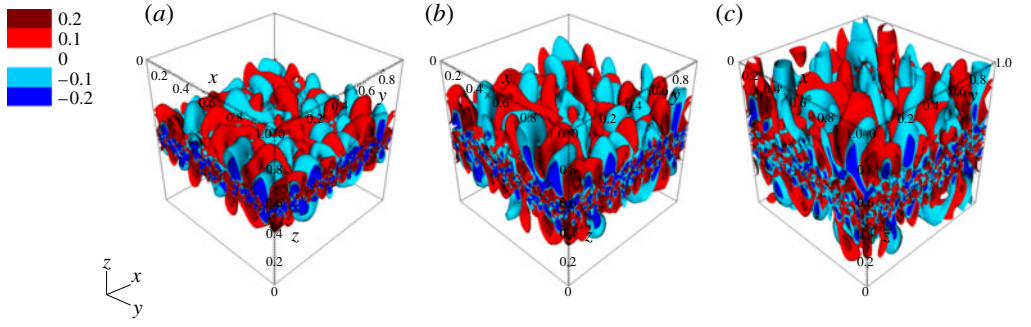


FIGURE 8. Isosurfaces of u_z at (*a*) $2\Omega t = 4$, (*b*) $2\Omega t = 8$ and (*c*) $2\Omega t = 12$ for the case R0.3 (red and blue colours respectively denote the positive and negative values of u_z).

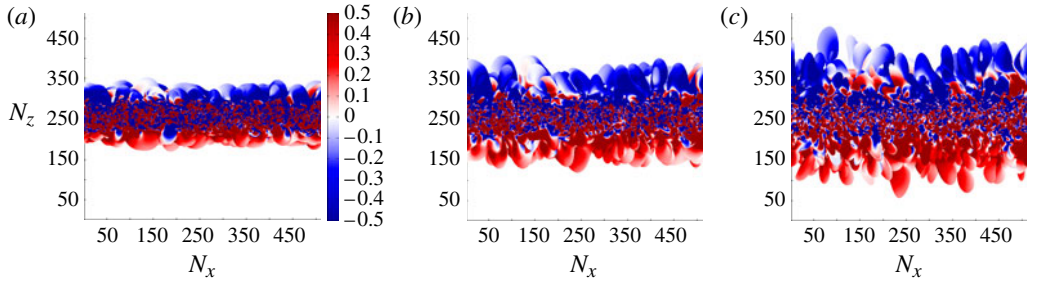


FIGURE 9. The isosurfaces of $u_z{}^2 = 0.05$ (front view) coloured with helicity (red denotes positive helicity and blue denotes negative) at (*a*) $2\Omega t = 4$, (*b*) $2\Omega t = 8$ and (*c*) $2\Omega t = 12$ for the case R0.3.

https://doi.org/10.1017/jfm.2014.457 Published online by Cambridge University Press

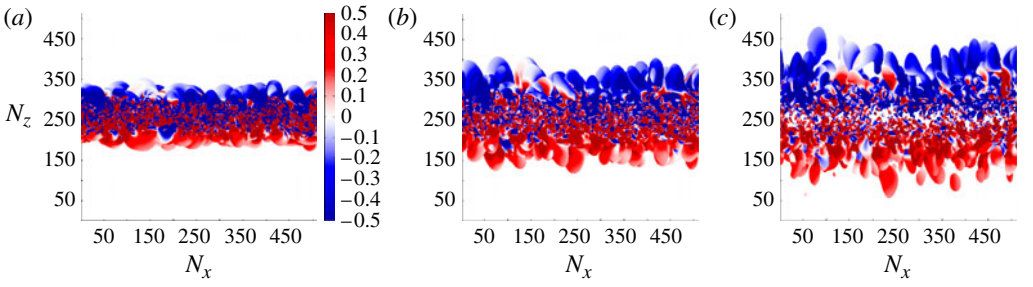


FIGURE 10. The isosurfaces of $u_z{}^2 = 0.05$ (front view) coloured with helicity (red denotes positive helicity and blue denotes negative) at (*a*) $2\Omega t = 4$, (*b*) $2\Omega t = 8$ and (*c*) $2\Omega t = 12$ for the case R0.5.

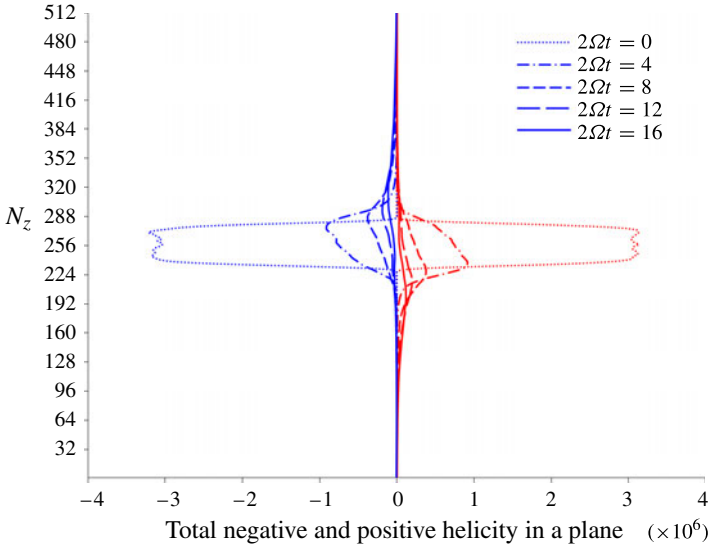


FIGURE 11. Total negative and positive helicity in horizontal planes $1 < N_z < 512$, where $N_z = N(z/2\pi)$ (red denotes positive helicity and blue denotes negative) for the case R0.3.

thickness. The maximum wave-cloud thickness is the distance between the fastest elongating structures along the $\pm z$-axis, while the mean wave-cloud thickness is defined in terms of the mean displacements of all columnar structures in the $\pm z$ direction, as indicated in figure 12(*a*). Figure 12(*b*) shows a linear rate of rise in both maximum and mean wave-cloud thicknesses indicating that the flow structures grow linearly with time. The linear elongation of columnar flow structures is also observed for cases R0.3 and R0.5. Moreover, the data points almost overlap for three cases considered, both for the mean and maximum thickness, when the z-, t-axes are non-dimensionalized by l_0 and Ω, respectively. This indicates that the columnar structures grow at the rate Ωl_0, which is consistent with the group velocity of waves. Let us consider this aspect in more detail.

In the isosurface plots discussed earlier it is observed that some of the columnar structures reach the box boundary earlier than others. These are the structures with larger characteristic width and thus have a higher group speed in accordance with

https://doi.org/10.1017/jfm.2014.457 Published online by Cambridge University Press

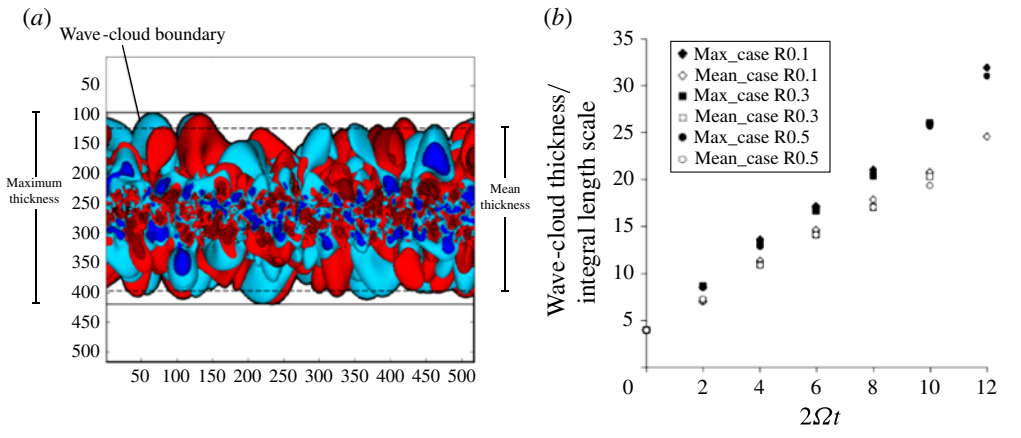


FIGURE 12. (Colour online) (*a*) Estimating the wave-cloud thickness using boundary tracking applied to velocity isosurfaces. (*b*) The maximum and mean wave-cloud thicknesses for cases R0.l, R0.3 and R0.5, with time.

$C_g = 2\Omega/k_\perp$. Here we provide quantitative evidence of this observation. We take a 2D DFT of the u_z velocity component in a particular horizontal (x–y) plane for the case R0.1. For example, for our purpose, we choose the planes corresponding to $z_1 = 0.75(2\pi)$ and $z_2 = 0.875(2\pi)$ above the cloud, and $z_1' = 0.25(2\pi)$ and $z_2' = 0.125(2\pi)$ below the cloud, as shown in figure 13. The spectral energy in the u_z component of velocity can be written as $E_z(k_\perp, t) = |\hat{u}_{2D,z}(k_\perp, t)|^2/2$, where $k_\perp = (k_x{}^2 + k_y{}^2)^{1/2}$. For the four planes, a spectrum plot of $2\Omega t$ versus $k_\perp$ with contours of $\log(E_z)$ is shown in figure 14. It shows the energy content in different wavenumbers during the period $2\Omega t = 0$–16. It is evident that the larger flow structures (with smaller $k_\perp$) have more energy and so are more prominent than the smaller ones. Moreover, it is interesting to see that the energy passing through a given plane moves progressively to the higher wavenumbers in accordance with the relationship: distance travelled $\approx 2\Omega t/k_\perp$. Note that the spectrum plots look almost identical for the corresponding planes above or below the cloud at the same vertical distance, indicating a symmetry in the elongation of columnar structures (see figure 14*c*, *d*). The distance travelled by the mid-plane of a wavepacket with mean wavenumber $k_\perp$ can be written as $\Delta z = C_g t = 2\Omega t/k_\perp$. The straight lines slopes given by $\Delta z_1 = 0.195(2\pi)$ and $\Delta z_2 = 0.32(2\pi)$ denote the time of flight (to the corresponding plane) of the mid-points of the inertial wavepackets with wavenumber $k_\perp$. These lines are shown in white in figure 14(*a*,*b*), respectively. The lower black line in these plots indicates that energy crosses a given plane ahead of the centre of a wavepacket.

The spectrum plots for other two cases, namely R0.3 and R0.5, in the four planes are almost identical (not shown here). The observations and inferences are, therefore, the same as discussed above. The planes under consideration are in the wave region, and the elongation rate or the size of columnar structures is unaffected by an increase in *Ro*. However, an increase in *Ro* results in a higher turbulent advection within the turbulent cloud, a point discussed at length in the subsequent section.

3.3. *Lagrangian particle tracking*

Lagrangian particle tracking is carried out to estimate the extent of turbulent advection so that the 'wave-only' region can be distinguished from the turbulent cloud. 65 536

https://doi.org/10.1017/jfm.2014.457 Published online by Cambridge University Press

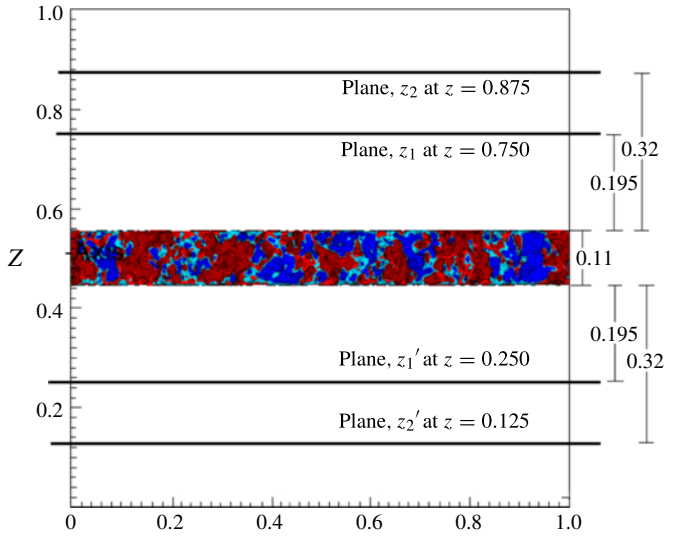


FIGURE 13. (Colour online) Location of reference planes: (*a*) $z_1 = 0.75$, (*b*) $z_2 = 0.875$, (*c*) $z_1' = 0.25$ and (*d*) $z_2' = 0.125$. All distances are non-dimensionalized by the box length 2π.

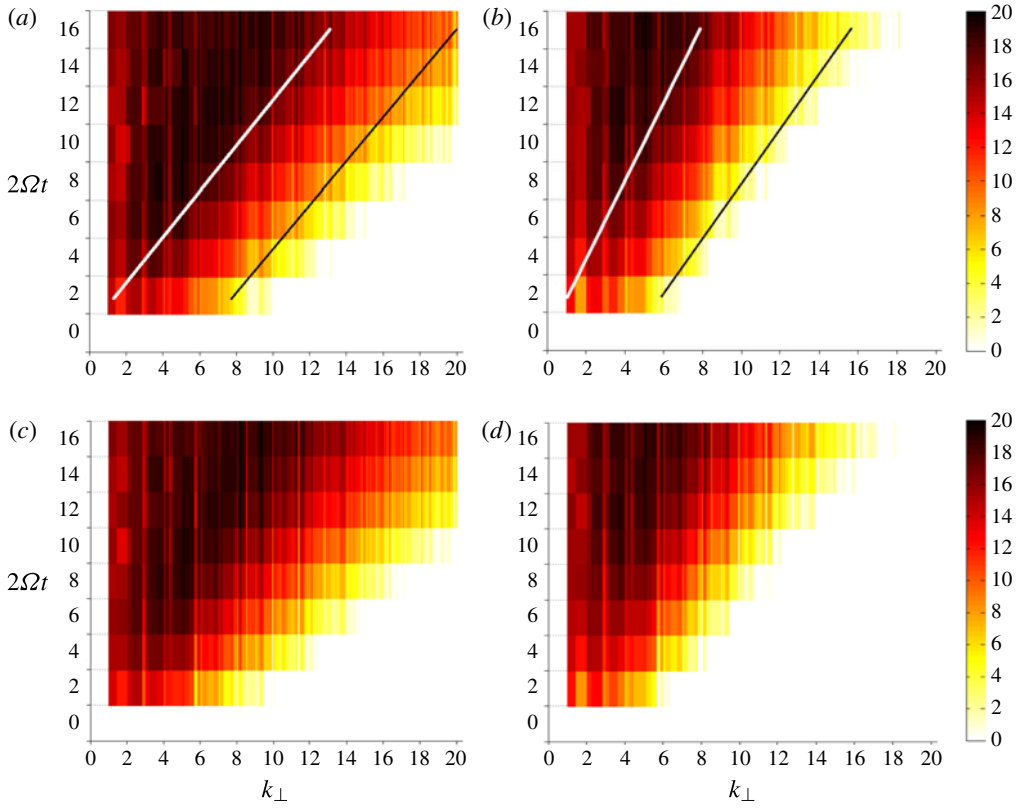


FIGURE 14. (Colour online) Plot of $2\Omega t$ versus $k_\perp$ with contours of $\log(E_z)$ for the plane (*a*) z_1, (*b*) z_2, (*c*) z_1' and (*d*) z_2'. The white straight lines indicate the time of flight to the corresponding plane.

https://doi.org/10.1017/jfm.2014.457 Published online by Cambridge University Press

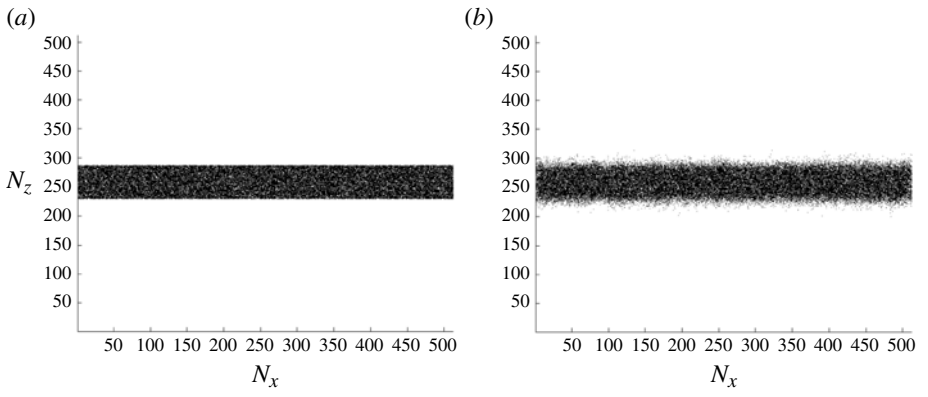


FIGURE 15. Particle distributions at (*a*) $2\Omega t = 0$ and (*b*) $2\Omega t = 16$ (front-view) for the case R0.1.

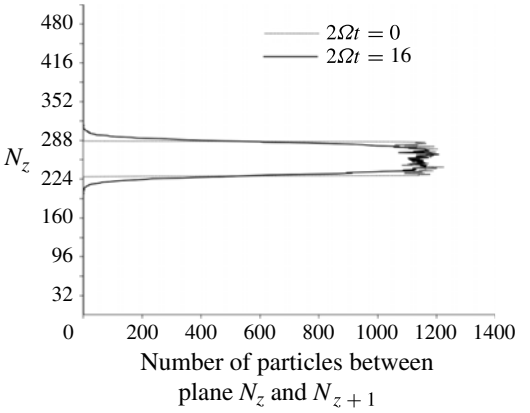


FIGURE 16. Particle number density in the adjacent horizontal planes at $2\Omega t = 0, 16$ for the case R0.1.

particles without inertia are uniformly and randomly distributed throughout the initial turbulent cloud (figure 4*a*). The particle position $\boldsymbol{r}$ at time t is determined using $\mathrm{d}\boldsymbol{r}/\mathrm{d}t = \boldsymbol{u}(\boldsymbol{r}, t)$. (Interpolation is used to find $\boldsymbol{u}$ if the particle is between grid points.) For the case R0.1, snapshots of the particle displacement at $2\Omega t = 0, 16$ are shown in figure 15(*a*, *b*) respectively. Since the *Ro* is rather low, the turbulent transport of particles is significantly less than the rate of elongation of columnar structures, confirming that the columnar structures cannot be due to turbulence. A quantitative picture of the particle displacement emerges from figure 16, where the number of particles between two adjacent horizontal planes corresponding to N_z and N_{z+1}, i.e. the particle number density, is plotted at $2\Omega t = 0, 16$, where $N_z = 512(z/2\pi)$. The horizontal planes corresponding to $N_z = 229$ and 286 denote the initial extent of the turbulent cloud (at $2\Omega t = 0$) and are designated as the reference planes for calculating the net particle displacement. The number of particles displaced above the cloud ($N_z > 286$) and below the cloud ($N_z < 229$) with time are plotted in figure 17(*a*). Using the total displacement of all particles above/below the reference planes, the r.m.s. of the particle displacements above/below is estimated and plotted

https://doi.org/10.1017/jfm.2014.457 Published online by Cambridge University Press

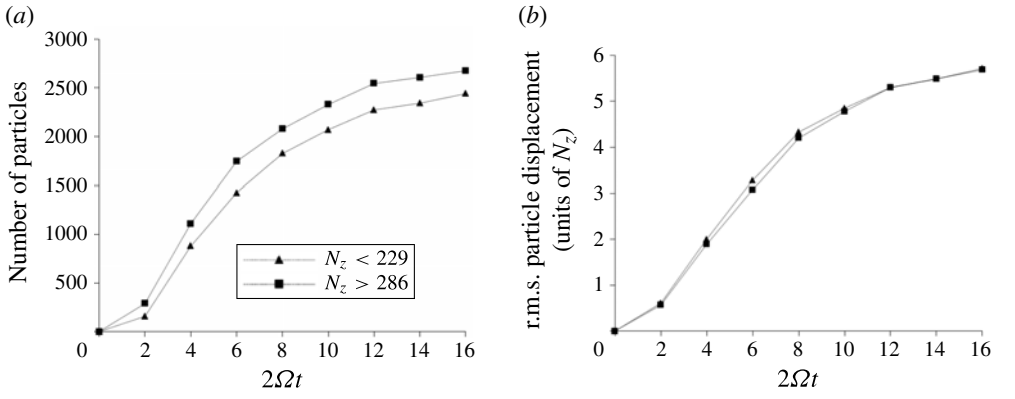


FIGURE 17. (*a*) Total number of particles above and below the reference planes and (*b*) r.m.s. particle displacement with time (for the case R0.1).

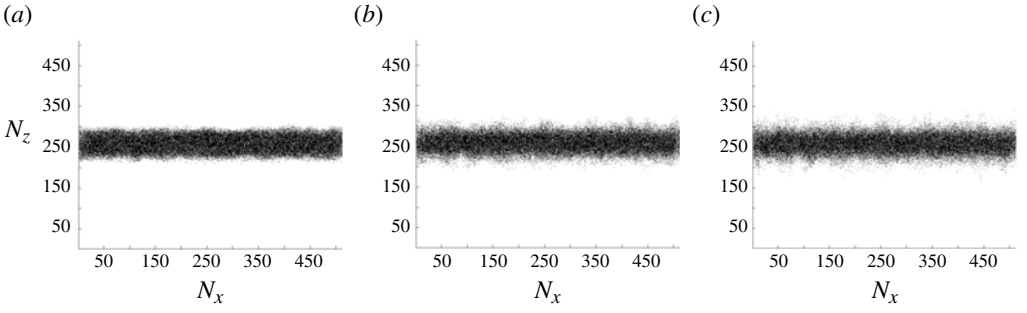


FIGURE 18. Particle distributions at (*a*) $2\Omega t = 4$, (*b*) $2\Omega t = 8$ and (*c*) $2\Omega t = 12$ (front view) for the case R0.3.

in figure 17(*b*). This r.m.s. displacement at a particular time denotes the extent of turbulent advection relative to the initial turbulent cloud. It is observed that the rate of increase in the r.m.s. displacement reduces with time. This is in part due to dissipation in kinetic energy.

Particle tracking is used for the other two cases, i.e. R0.3 and R0.5, as well and the r.m.s. particle displacement is estimated. Particle distributions at (*a*) $2\Omega t = 4$, (*b*) $2\Omega t = 8$ and (*c*) $2\Omega t = 12$ (the front-view) for the cases R0.3 and R0.5 are shown in figures 18 and 19, respectively. The particle number densities for these two cases are shown in figure 20(*a*,*b*) at $2\Omega t = 0, 16$, respectively. The extent of turbulent advection is higher than in the case R0.1, and there is a notable drop in particle density in the cloud region for the case R0.5. The corresponding r.m.s. displacements for the cases R0.3 and R0.5 are shown in figure 21(*a*,*b*) respectively. The r.m.s. displacement becomes nearly constant for $2\Omega t > 12$ indicating that there is little significant advection after a certain time.

3.4. *Wave energetics*

How much energy do the inertial waves carry away from the turbulent cloud? To address this, we must first distinguish the wave-only region from the turbulent cloud. The r.m.s. particle displacement estimated in the previous section (§ 3.3) is used

https://doi.org/10.1017/jfm.2014.457 Published online by Cambridge University Press

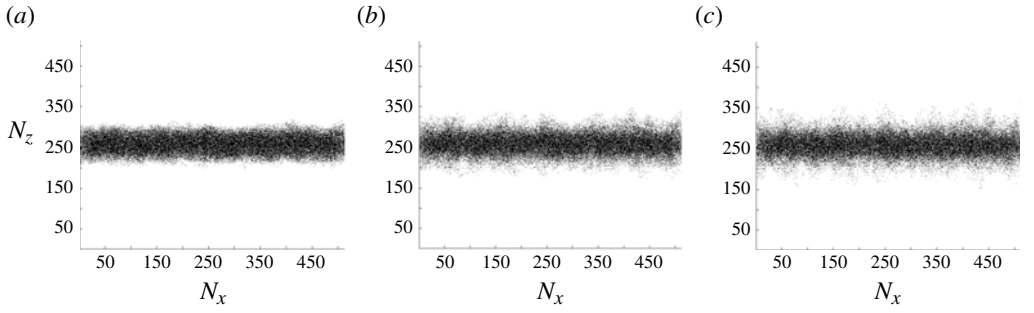


FIGURE 19. Particle distributions at (*a*) $2\Omega t = 4$, (*b*) $2\Omega t = 8$ and (*c*) $2\Omega t = 12$ (front view) for the case R0.5.

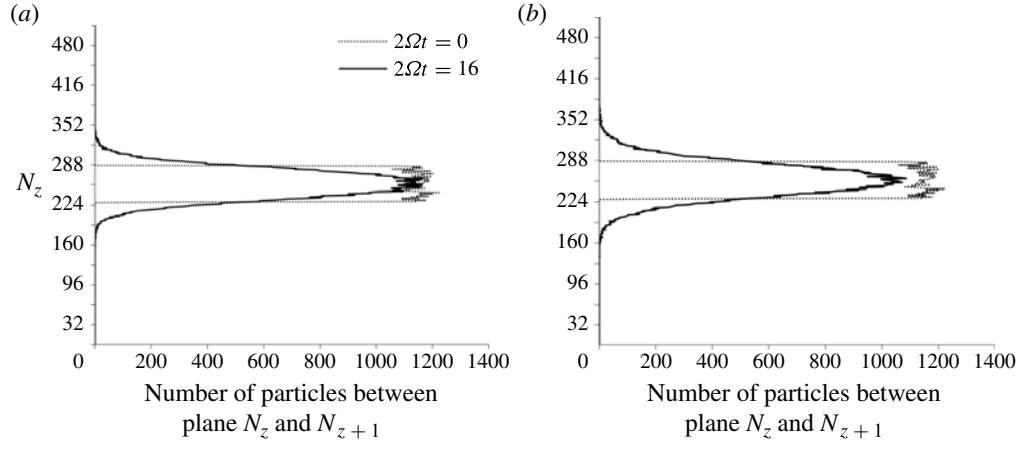


FIGURE 20. Particle number density in the adjacent horizontal planes for the cases (*a*) R0.3 and (*b*) R0.5 at $2\Omega t = 0, 16$.

for this purpose. For example, at $2\Omega t = 16$, the r.m.s. particle displacement is 6 (N_z units) on both sides of the cloud for the case R0.1 (figure 17*b*). The reference planes are $N_z = 229$ and 286 and so the extent of the turbulent cloud is said to be from $N_z = 229 - 6 = 223$ to $N_z = 286 + 6 = 292$ at $2\Omega t = 16$. In such a case, the total kinetic energy in the region defined by $0 < N_z < 223$ and $292 < N_z < 512$ is the energy in the inertial waves which have propagated out of the turbulent cloud in the period $2\Omega t = 0, 16$. The same method is used to distinguish the wave-only region at other times, and then to estimate the kinetic energy in the waves.

The kinetic energy, averaged in the horizontal plane, $u^2/2$ is plotted in figure 22 for all of the horizontal planes ($1 < N_z < 512$). In the central plane ($N_z = 256$), the kinetic energy falls rapidly due to viscous dissipation, in addition to advection and transfer to the inertial waves. The amount of energy transferred to the waves with time is plotted in figure 23. It is observed that up to $2\Omega t = 16$, approximately 40 % of the initial kinetic energy in turbulence is transferred to the waves, while 43 % is dissipated. Moreover, at $2\Omega t = 16$, 70 % of the total kinetic energy is present in inertial waves. This confirms that the inertial waves are an efficient means of energy dispersion. The energy carried away by inertial waves at higher *Ro* is listed

https://doi.org/10.1017/jfm.2014.457 Published online by Cambridge University Press

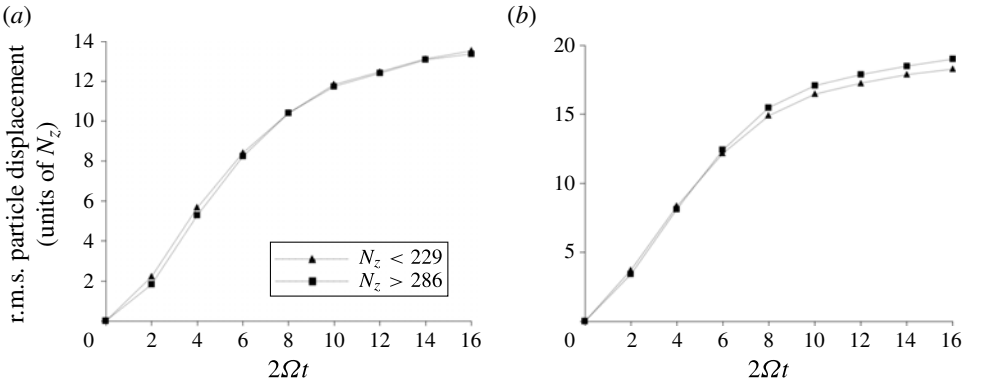


FIGURE 21. Root-mean-square particle displacement with time for the cases (*a*) R0.3 and (*b*) R0.5.

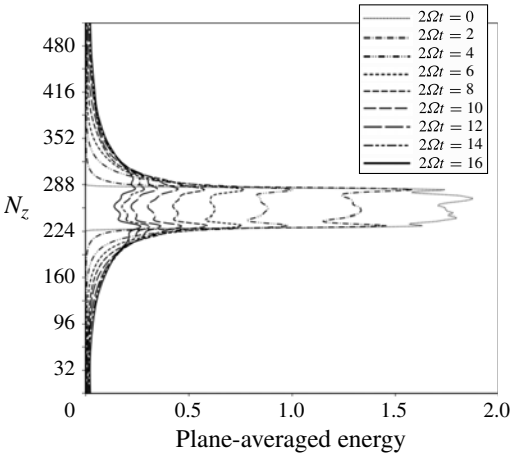


FIGURE 22. Plane-averaged kinetic energy for the case R0.1.

in table 3. It is evident that the net amount of energy carried away by the waves is lower at higher *Ro*. However, the percentage of total kinetic energy present in the waves increases with *Ro* (table 3*b*). This is due to a higher energy dissipation rate at larger *Ro*.

3.5. *Enstrophy in the waves*

The enstrophy carried away by inertial waves can be determined, using the r.m.s. particle displacement method (discussed in § 3.4) to distinguish the wave-only region from turbulence. For example, the enstrophy in the region defined by $0 < N_z < 223$ and $292 < N_z < 512$ is the enstrophy in the inertial waves which have propagated out of the turbulent cloud in the period $2\Omega t = 0, 16$. It is observed (figure 24) that waves carry very little, only 6.5 % of the initial, enstrophy in the turbulent cloud in $2\Omega t = 0 - 16$ for the case R0.1. Most of the initial enstrophy, approximately 79.4 %, is dissipated. This is because the inertial waves are mostly associated with length scales much larger than the small-scale turbulence where

https://doi.org/10.1017/jfm.2014.457 Published online by Cambridge University Press

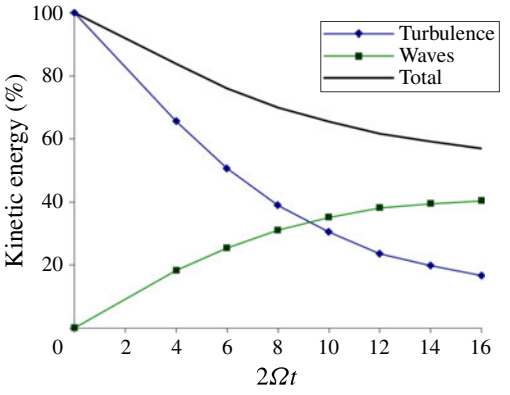


FIGURE 23. (Colour online) Total kinetic energy in the inertial waves and turbulence, for the case R0.1.

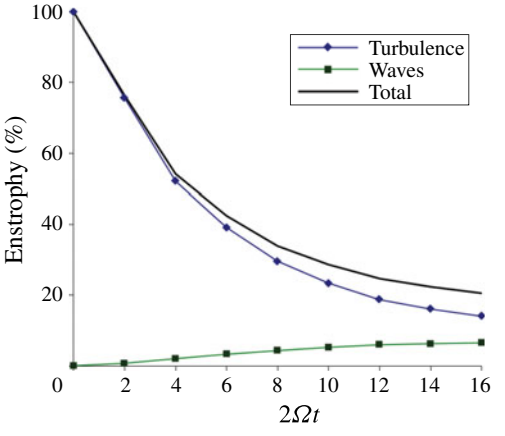


FIGURE 24. (Colour online) Enstrophy in the inertial waves and turbulence for the case R0.1.

Case		$2\Omega t = 4$	$2\Omega t = 8$	$2\Omega t = 12$	$2\Omega t = 16$
R0.1	(*a*)	18.3	31.1	38.1	40.3
	(*b*)	21.8	44.4	61.8	70.8
R0.3	(*a*)	12.9	19.4	22.4	22.8
	(*b*)	24.2	50.5	69.6	79.3
R0.5	(*a*)	9.61	13.9	15.6	15.6
	(*b*)	25.3	54.7	74.3	82.9

TABLE 3. (*a*) Percentage of initial kinetic energy in the waves. (*b*) Percentage of total kinetic energy in the waves at a particular time.

most of the enstrophy is held. The enstrophy transferred to the waves is even lower at higher *Ro*, and becomes constant with increasing time, as can be observed in table 4.

https://doi.org/10.1017/jfm.2014.457 Published online by Cambridge University Press

Case		$2\Omega t = 4$	$2\Omega t = 8$	$2\Omega t = 12$	$2\Omega t = 16$
R0.1	(*a*)	2.05	4.31	5.98	6.52
	(*b*)	3.80	12.7	24.2	31.7
R0.3	(*a*)	1.36	1.64	1.86	1.86
	(*b*)	5.40	17.5	39.6	59.8
R0.5	(*a*)	0.89	0.87	0.92	0.92
	(*b*)	6.40	21.3	46.6	66.6

TABLE 4. (*a*) Percentage of initial enstrophy in the waves. (*b*) Percentage of total enstrophy in waves at a particular time.

4. Conclusions

The evolution of a localized turbulent cloud under rotation has been studied using DNS in a periodic box. For all three cases considered, namely R0.1, R0.3 and R0.5, we observe that columnar structures spontaneously emerge from the turbulent cloud and grow towards the box boundary. These are observed to be qualitatively similar to the structures seen in the visualizations of Davidson *et al.* (2006). It is confirmed that these structures are formed by the inertial waves. This stems from our observation that most columnar structures moving along the $+z$ have negative helicity and those moving along the $-z$ direction have positive helicity, a characteristic typical of inertial waves. In addition, we find that these structures elongate linearly with non-dimensional time Ωt. This picture is further confirmed by the spectrum plots and by the Lagrangian particle tracking. These results confirm the observations of Davidson *et al.* (2006) and Kolvin *et al.* (2009). It is interesting to note that the spontaneous emergence of columnar structures observed in the present study is similar to that observed by Godeferd & Lollini (1999) in presence of confinement at low Re. This indicates that fast linear dynamics prevails over slow nonlinear dynamics in the short time scale (corresponding to Coriolis force or Ekman pumping) at $Ro \sim 0.1$, at least in the case of inhomogeneous turbulence under rotation. A clear bias in the helicity propagation direction exists even inside the turbulent cloud, which suggests that the linear wave propagation might play a role even in the case of homogeneous turbulence under rotation along with the nonlinear dynamics, a study which is outside the scope of the present work.

Particle tracking is used to determine the extent of the turbulent advection, which increases with an increase in Ro. It is difficult to clearly distinguish the waves and the turbulence regions where they spatially overlap. In this study, the 'wave-only' region is distinguished from the turbulent cloud using r.m.s. particle displacement. Thus, the amount of energy and enstrophy in the inertial waves can be estimated. The amount of kinetic energy transferred to the waves is 40 % of the initial at $Ro = 0.1$, and decreases with an increase in Ro to 23 and 16 % at $Ro = 0.3$ and 0.5, respectively. However, the percentage of total energy held by the waves increases with Ro. Therefore, inertial waves provide an efficient means of energy dispersion, particularly at low Ro. Our observation that inertial waves can carry a significant portion of the kinetic energy away from a localized turbulence under the effect of rotation, is of significance in the atmospheric or oceanic energy budgets.

Acknowledgements

The authors would like to thank Professor P. K. Yeung (Georgia Tech, US) for sharing his pseudo-spectral DNS code. A.R. wishes to thank Dr A. Maffioli for his useful inputs and discussions and St. John's college for the financial support.

https://doi.org/10.1017/jfm.2014.457 Published online by Cambridge University Press

REFERENCES

BARTELLO, P., MÉTAIS, O. & LESIEUR, M. 1994 Coherent structures in rotating three-dimensional turbulence. *J. Fluid Mech.* **29**, 1–29.

BELLET, F., GODEFERD, F. S., SCOTT, J. F. & CAMBON, C. 2006 Wave turbulence in rapidly rotating flows. *J. Fluid Mech.* **562**, 83–121.

BORDES, G., MOISY, F., DAUXOIS, T. & CORTET, P. 2012 Experimental evidence of a triadic resonance of plane inertial waves in a rotating fluid. *Phys. Fluids* **24** (1), 014105.

CAMBON, C. & JACQUIN, L. 1989 Spectral approach to non-isotropic turbulence subjected to rotation. *J. Fluid Mech.* **202**, 295–317.

CAMBON, C., MANSOUR, N. N. & GODEFERD, F. S. 1997 Energy transfer in rotating turbulence. *J. Fluid Mech.* **337**, 303–332.

DAVIDSON, P. A. 2013 *Turbulence in Rotating, Stratified and Electrically Conducting Fluids*. Cambridge University Press.

DAVIDSON, P. A. 2014 The dynamics and scaling laws of planetary dynamos driven by inertial waves. *Geophys. J. Int.* **198**, 1832–1847.

DAVIDSON, P. A., STAPLEHURST, P. J. & DALZIEL, S. B. 2006 On the evolution of eddies in a rapidly rotating system. *J. Fluid Mech.* **557**, 135–144.

DICKINSON, S. C. & LONG, R. R. 1983 Oscillating-grid turbulence including effects of rotation. *J. Fluid Mech.* **126**, 315–333.

DURAN-MATUTE, M., FLOR, J., GODEFERD, F. & JAUSE-LABERT, C. 2013 Turbulence and columnar vortex formation through inertial-wave focusing. *Phys. Rev.* E **87** (4), 041001.

GODEFERD, F. S. & LOLLINI, L. 1999 Direct numerical simulations of turbulence with confinement and rotation. *J. Fluid Mech.* **393**, 257–308.

GREENSPAN, H. P. 1968 *The Theory of Rotating Fluids*. Cambridge University Press.

HAINE, T. W. H. & CHERIAN, D. A. 2013 Analogies of ocean/atmosphere rotating fluid dynamics with gyroscopes: teaching opportunities. *Bull. Am. Meteorol. Soc.* **94**, 673–684.

HOPFINGER, E. J., BROWAND, F. K. & GAGNE, Y. 1982 Turbulence and waves in a rotating tank. *J. Fluid Mech.* **125**, 505–534.

JACQUIN, L., LEUCHTER, O., CAMBON, C. & MATHIEU, J. 1990 Homogeneous turbulence in the presence of rotation. *J. Fluid Mech.* **220**, 1–52.

KOLVIN, I., COHEN, K., VARDI, Y. & SHARON, E. 2009 Energy transfer by inertial waves during the buildup of turbulence in a rotating system. *Phys. Rev. Lett.* **102** (1), 1–4.

LIGHTHILL, M. J. 1967 On waves generated in dispersive systems by travelling forcing effects, with applications to the dynamics of rotating fluids. *J. Fluid Mech.* **27** (4), 725–752.

LILLY, D. K. 1986 The structure, energetics and propagation of rotating convective storms. Part II: helicity and storm stabilization. *J. Atmos. Sci.* **43**, 126–140.

MAFFIOLI, A., DAVIDSON, P. A., DALZIEL, S. B. & SWAMINATHAN, N. 2014 The evolution of a stratified turbulent cloud. *J. Fluid Mech.* **739**, 229–253.

MININNI, P. D. & POUQUET, A. 2010 Rotating helical turbulence. I. Global evolution and spectral behavior. *Phys. Fluids* **22**, 035135.

MOFFATT, H. K. 1970 Dynamo action associated with random inertial waves in a rotating conducting fluid. *J. Fluid Mech.* **44** (4), 705–719.

NAZARENKO, S. V. & SCHEKOCHIHIN, A. A. 2011 Critical balance in magnetohydrodynamic, rotating and stratified turbulence: towards a universal scaling conjecture. *J. Fluid Mech.* **677**, 134–153.

OLSON, P. 2013 Experimental dynamos and the dynamics of planetary cores. *Annu. Rev. Earth Planet. Sci.* **41**, 153–181.

PAN, C. 2001 Gibbs phenomenon removal and digital filtering directly through the fast Fourier transform. *IEEE Trans. Signal Process.* **49** (2), 444–448.

PROUDMAN, J. 1916 On the motion of solids in a liquid possessing vorticity. *Proc. R. Soc. Lond.* A **92**, 408–424.

ROGALLO, R. S. 1981 Numerical experiments in homogeneous turbulence. *Tech Rep.* 81835. NASA Technical Memorandum.

SCOTT, J. F. 2014 Wave turbulence in a rotating channel. *J. Fluid Mech.* **741**, 316–349.

https://doi.org/10.1017/jfm.2014.457 Published online by Cambridge University Press

SMITH, L. M. & LEE, Y. 2005 On near resonances and symmetry breaking in forced rotating flows at moderate Rossby number. *J. Fluid Mech.* **535**, 111–142.

SMITH, L. M. & WALEFFE, F. 1999 Transfer of energy to two-dimensional large scales in forced, rotating three-dimensional turbulence. *Phys. Fluids* **11** (6), 1608–1622.

STAPLEHURST, P. J. 2007 Structure formation in rotating turbulence. PhD thesis, Department of Engineering, University of Cambridge.

STAPLEHURST, P. J., DAVIDSON, P. A. & DALZIEL, S. B. 2008 Structure formation in homogeneous freely decaying rotating turbulence. *J. Fluid Mech.* **598**, 81–105.

TAYLOR, G. I. 1921 Experiments with rotating fluids. *Proc. R. Soc. Lond.* A **100** (73), 114–121.

THOMPSON, R. O. R. Y. 1978 Observation of inertial waves in the stratosphere. *Q. J. R. Meteorol. Soc.* **104** (441), 691–698.

VERONIS, G. 1970 The analogy between rotating and stratified fluids. *Annu. Rev. Fluid Mech.* **2**, 37–66.

WALEFFE, F. 1993 Inertial transfers in the helical decomposition. *Phys. Fluids* A **5** (3), 677–685.

WILSON, J. D., THURTELL, G. W. & KIDD, G. E. 1981 Numerical simulation of particle trajectories in inhomogeneous turbulence, II: systems with variable turbulent velocity scale. *Boundary-Layer Meteorol.* **21**, 423–441.

YEUNG, P. K. & ZHOU, Y. 1998 Numerical study of rotating turbulence with external forcing. *Phys. Fluids* **10** (11), 2895–2909.

YOSHIMATSU, K., MIDORIKAWA, M. & KANEDA, Y. 2011 Columnar eddy formation in freely decaying homogeneous rotating turbulence. *J. Fluid Mech.* **677**, 154–178.

ZHEMIN, T. & RONGSHENG, W. 1994 Helicity dynamics of atmospheric flow. *Adv. Atmos. Sci.* **11** (2), 175–188.

https://doi.org/10.1017/jfm.2014.457 Published online by Cambridge University Press